frontiers | Frontiers in Built Environment

TYPE Original Research
PUBLISHED 19 September 2022
DOI 10.3389/fbuil.2022.1020217



OPEN ACCESS

EDITED BY
Xiaohong Zhu,
Hong Kong Polytechnic University,
Hong Kong SAR, China

REVIEWED BY
Ning Li,
University of Glasgow, United Kingdom
Jie Ren,
University of Colorado Boulder,
United States
Yuyan Huang,
University of Leeds, United Kingdom

*CORRESPONDENCE
Bo Fu,
2015006@nmu.edu.cn

SPECIALTY SECTION
This article was submitted to
Construction Materials,
a section of the journal
Frontiers in Built Environment

RECEIVED 16 August 2022
ACCEPTED 09 September 2022
PUBLISHED 19 September 2022

CITATION
Zhan J, Li H, Li H, Cheng Z and Fu B
(2022), Composition design and
characterization of alkali-activated
Slag–Metakaolin materials.
*Front. Built Environ.* 8:1020217.
doi: 10.3389/fbuil.2022.1020217



# Composition design and characterization of alkali-activated Slag–Metakaolin materials

Jianghuai Zhan[1], Hongbo Li[2], Huang Li[3], Zhenyun Cheng[1] and Bo Fu[1,4]*

[1]School of Civil Engineering, North Minzu University, Yinchuan, China, [2]College of Civil and Hydraulic Engineering, Ningxia University, Yinchuan, China, [3]China Construction Fifth Engineering Bureau Co.,ltd, ChangSha, China, [4]National Energy Group, Coal Chemical Industry Technology Research Institute, Ningxia Coal Industry Co. Ltd., Yinchuan, China

This study explores the effects of the interactions among $Na_2O$ content, metakaolin content and activator modulus on the compressive strength and autogenous shrinkage of alkali-activated slag–metakaolin (AASM) materials. The Box–Behnken RSM design was used to create an experimental scheme, establish a model, and optimize the mix proportions. Fourier transform infrared spectroscopy, scanning electron microscopy, and Mercury intrusion experiments were used to analyze the compositions, microstructures, and pore structures of the hydration products of the AASM, respectively. Results showed that the interactions between the activator modulus and metakaolin content, as well as $Na_2O$ content and metakaolin content, are the key factors affecting the compressive strength and autogenous shrinkage, respectively, of the AASM. Under the optimal conditions of $Na_2O$ content of 6%, sodium silicate modulus of 1.5, and metakaolin/slag ratio of 1: 3, the relative errors in the model verification test for compressive strength and autogenous shrinkage are 0% and 0.18%, respectively. In the water glass modulus and metakaolin content interaction, $Ca^{2+}$, $A1^{3+}$, and $Si^{4+}$ ions in the composite system react with several $[SiO_4]^{4-}$ groups to form C-A-S-H and N-A-S-H gels, which fill each other to make the composite structure denser. When $Na_2O$ interacts with metakaolin, the $OH^-$ and $Na^+$ in the solution react with $A1^{3+}$ and $Si^{4+}$ to generate additional N-A-S-H, thereby reducing the compressive strength of the composite system, mitigating autogenous shrinkage, and increasing volume stability.

KEYWORDS

**AASM material, response surface, compressive strength, autogenous shrinkage, microscopic analysis**

# 1 Introduction

With the rapid development of the world economy, Portland cement is widely used in roads, bridges, buildings, oceans, water conservancy, and other engineering applications, and the demand is rising. Cement production increased from $5.93 \times 10^8$ t in 2000 to $23.63 \times 10^8$ t in 2021, with an average annual growth rate of approximately 27.13% (Sui and Liu, 2013; Li et al., 2020). However, the production of Portland cement consumes considerable energy and emits a large amount of $CO_2$, which causes tremendous pressure on the environment and natural resources. In China's dual-carbon strategy, using industrial by-products, such as slag and fly ash, in place of cement is a critical way to reduce $CO_2$ emissions.

Alkali-activated materials, a new type of cementitious material with good durability and environmentally friendly, are prepared using an alkaline activator and aluminosilicate with mineral or industrial by-products, such as milled slag powder and fly ash (Li et al., 2018; Ren et al., 2020; Zhan et al., 2022). Compared with Portland cement, alkali-activated materials have excellent performance and low environmental load (Provis, 2013; Li et al., 2017a; Chen et al., 2021; Zhu et al., 2021; Ren et al., 2022a). Therefore, the preparation of concrete using alkali-activated materials is an important means of energy conservation and emission reduction in civil engineering and sustainable development. Alkali-activated materials can be divided into two categories according to their reaction products: (1) alkali-activated high-calcium materials (such as alkali-activated slag), which have type I C (-A)-S-H gel as the main reduction product, and (2) alkali-activated low-calcium materials (such as alkali-activated fly ash and metakaolin), which have amorphous aluminum silicate hydrate (N-A-S-H) gel as the main reaction product (Zhu et al., 2018). Alkali-activated high-calcium materials have high strength, but have a short setting time and poor volume stability. Alkali-activated low-calcium materials have a long setting time, good volume stability, and excellent durability but have low strength. Therefore, the combination of alkali-activated high-calcium cementitious materials and low-calcium cementitious materials can enable the two types of materials to complement each other in performance (Pu, 2010). Jiang (2016), Chen (2018), Luo (2016), and Parveen et al. (2019) studied alkali-activated slag–metakaolin cement and found that the setting time of paste was significantly shortened with an increase in slag content. Yip et al. (2004) found that the compressive strength of slag–metakaolin materials increased and then decreased with increased slag content. They exhibited the highest compressive strength when the mass fraction of slag was 40 wt%. Yang et al. (2015) obtained the optimal strength, density, and pore structure of slag–metakaolin composite system when the slag content was 50%. Peng et al. (2020) and Cui et al. (2017) showed that a metakaolin/slag mass ratio of 6:4 yielded the highest compressive strength of geopolymer paste and a high reaction level. Fu et al. (2021) found that the addition of metakaolin to slag could coarsen the pore structure of a hardened body, thereby reducing the autogenous shrinkage and drying shrinkage of alkali-activated slag. As for activators, Burciaga-Díaz et al. (2013) and Ma et al. (2019) found that the compressive strength of metakaolin–slag geopolymer paste with different slag contents increased and then decreased with an increase in modulus, and there were different optimal modulus values. In the study of Fu et al. (2018), an alkali activator with a high alkali ion concentration did not form stable reaction products when it reacted with solid raw materials, thus decreasing the compressive strength of oligomer paste. Zhan et al. (2022) found that when the $Na_2O$ content was between 8% and 12%, a rise in alkali content led to the drying and contraction of alkali-activated metakaolin geopolymers and an increase in autogenous and chemical shrinkage. As stated by Wang et al. (2008), alkali-activated metakaolin cementitious materials performed well with a 1.0 modulus of sodium silicate and 8% $Na_2O$ content. Regarding mix proportion optimization, Abdelaziz et al. (2019) concluded that slag-based polymers performed the best at a GBFS/metakaolin ratio of 1, [GBFS + metakaolin]/activator ratio of 3, and modulus of sodium silicate of 1.6–1.8; they also stated that the modulus of sodium silicate considerably influenced the performance of the slag-based polymers. The cementitious material of Chi and Huang (2013) exhibited the highest strength at a fly ash/slag mass ratio of 1, sodium silicate modulus of 1.0, $Na_2O$ content of 6%, and water/cement ratio of 0.5. Zheng and Zhu (2015) obtained the optimal ratio of alkali-activated slag cementitious materials when water consumption was 35% and 42% of the slag mass, the water glass consumption was 12% of the slag mass, and the water glass modulus was 1.0. Davidovits (1989) found that 3.5–4.5, 0.2–0.48, and 10–25 were the best ratios of the alkali-activated metakaolin cementitious materials n $(SiO_2)$/n $(Al_2O_3)$, n $(Na_2O)$/n $(SiO_2)$, and n $(Na_2O)$/n $(H_2O)$, respectively. As reported by Barbosa et al. (2000), 3.8, 0.25, and 10 were the best n $(SiO_2)$/n $(Al_2O_3)$, n $(Na_2O)$/n $(SiO_2)$, and n $(H_2O)$/n $(Na_2O)$ ratios, respectively.

Different methods have been used to construct performance prediction models of alkali-activated materials. Zhong et al. (2021) used the lasso algorithm to establish a macro performance prediction model of metakaolin–slag geopolymer paste; the correlation coefficient between the predicted and experimental values was greater than 0.92. Liu et al. (2021) used RSM to optimize and model the ratio of paste composite filling and determined 30: 15: 1: 50: 4 as the optimal cement/lime/gypsum/slag/calcium formate ratio. At this time, the relative errors in their model verification test were 3.25% and 0.93%; both were less than 5%, indicating that the model had high accuracy and strong reliability. Yang et al. (2016) and Zhang et al. (2013) used BP neural networks to establish a prediction model and optimize the optimal ratio of cementitious composite materials. Khan et al. (2020) used response surface methodology (RSM) to design the optimization and statistical modeling of cement paste containing

irradiated plastic waste and silica fume. Zhou et al. (2022) used RSM to optimize the performance of desulfurization-gypsum-based cementitious composite materials. Results showed that the optimal proportions of sulfoaluminate cement, mineral powder, and quicklime were 7.82%, 21%, and 5.22%, respectively. With these proportions, the composites had excellent strength and water resistance. Gao et al. (2016) used RSM to optimize slag alkali-activated cementitious materials' design and statistical modeling. According to their findings, when the modulus of the alkali activator was 1.0–1.4, the mass fraction of the alkali activator was 25%–30%. The mass ratio of the activator to solid was 0.50, the components in the slag alkali-activated cementitious materials could fully play a synergistic role leading to an excellent early performance of the materials.

The setting/hardening mechanism of alkali-activated cementitious materials differs from that of ordinary portland cement (OPC). The former's ratio design and preparation theory is far less mature than those of the latter. In addition, setting time, early strength, and shrinkage are not easy to control when preparing alkali-activated cementitious materials. Thus, their raw materials, ratio schemes, and other aspects have been studied (Puertas et al., 2011; Li et al., 2013) to improve their performance. The single factor change method, which is used in most relevant studies, cannot reflect the interaction between various factors. The composition of alkali-activated cementitious composite systems is complex, and the influence of such interaction on their performance is remarkable (Susan et al., 2007; Frank et al., 2009). However, research on this interaction of factors is limited, and related mechanisms must be further studied.

This paper, selected main component parameters, such as $Na_2O$ content, modulus change, and metakaolin content, as influencing factors. RSM was used to design an experimental scheme systematically and analyze the results of alkali-activated slag–metakaolin (AASM) materials (Zhao, 2013). The factors and the influence laws of the interaction between each component on the compressive strength and autogenous shrinkage of AASM were clarified. FTIR, SEM, and MIP characterized the microstructure of the materials. The effects of factor interaction on the composition of hydration products, microstructure morphology, and pore structure of AASM were analyzed, thereby providing a theoretical basis for the composition design of AASM.

# 2 Materials and methods

## 2.1 Materials

### 2.1.1 Slag

In this study, slag (Ningxia Iron and Steel Group, Zhongwei City, China), a by-product of blast furnace ironmaking, was used as the main binder. Slag is mainly composed of calcium aluminate materials. Its density and specific surface area were 2890 $kgm^{-3}$ and 410 $m^2\,kg^{-1}$, respectively. The chemical composition and particle size distribution were determined by XRF and laser particle size analysis, respectively. The chemical composition and particle size distribution are shown in Table 1 and Figure 1, respectively.

### 2.1.2 Metakaolin

Metakaolin (Inner Mongolia Chaopai Company, Hohhot City, China) was used as a composite binder. It is a high-activity amorphous aluminosilicate material with kaolin clay calcined at 600°C–900°C. Its density and specific surface area were 2300 $kgm^{-3}$ and 800 $m^2\,kg^{-1}$, respectively, and its chemical composition and particle size distribution are shown in Table 1 and Figure 1, respectively. Metakaolin content replaces slag (0%, 25%, and 50% of raw material weight).

### 2.1.3 Alkaline activator

The alkaline activator was a solution composed of a sodium silicate solution, solid sodium hydroxide, and water. The sodium silicate solution used in this study (Linyi Lusen Chemical Co., Ltd., China) had a $SiO_2$ content of 29.94 wt%, $Na_2O$ content of 8.86 wt%, and water content of 61.9 wt%. Sodium hydroxide flakes with a purity of 99% (Ningxia Jinyuyuan Chemical Group Co., Ltd.) were used to adjust the modulus of sodium silicate. The water was deionized.

### 2.1.4 Experimental sand

Standard sand was used to prepare AASM. It was produced by Xiamen Aisiou Standard Sand Co., Ltd., and conformed to the GB/T 17671–1999 (1999) specification for cement mortar strength tests. Its particle diameter, specific gravity, and fineness modulus were 0.08–2 mm, 1.41, and 2.30, respectively. Specific gravity is the ratio of the substance density (fully dense state) to the density of 3.98°C pure water at standard atmospheric pressure. The fineness modulus is an index to characterize the degree and type of natural sand grain diameter.

## 2.2 Experimental design based on RSM

The Box–Behnken RSM design was used for the experimental design of cementitious composite systems. As shown in Figure 2A, the metakaolin content, alkali content ($Na_2O$ content), and modulus (Ms = $n$ ($SiO_2$)/n ($Na_2O$)) were selected as the ratio variables to design the experiment. The response values were the compressive strength ($Y_1$) and autogenous shrinkage ($Y_2$) of the AASM. According to References (Fu et al., 2010; Zarina et al., 2012) and a trial test, the primary variation ranges of the three variables were determined, and quadratic RSM was directly used for the experimental design. This method was used for 17 experiments, including a group of points and five central points at the midpoint of each side for error

TABLE 1 Chemical compositions of metakaolin and slag.

| Material | Oxide composition (wt%) | | | | | | | | | |
|---|---|---|---|---|---|---|---|---|---|---|
| | $K_2O$ | $Na_2O$ | $SO_3$ | $SiO_2$ | $Fe_2O_3$ | $Al_2O_3$ | MgO | CaO | $TiO_2$ | LOI |
| Slag | 0.83 | 0.73 | 0.13 | 35.88 | 0.46 | 10.65 | 11.43 | 33.54 | 1.14 | 1.30 |
| Metakaolin | 0.44 | 0.41 | — | 49.78 | 0.93 | 34.63 | 2.58 | — | 1.01 | 1.10 |

Notes: LOI, is the loss on ignition.

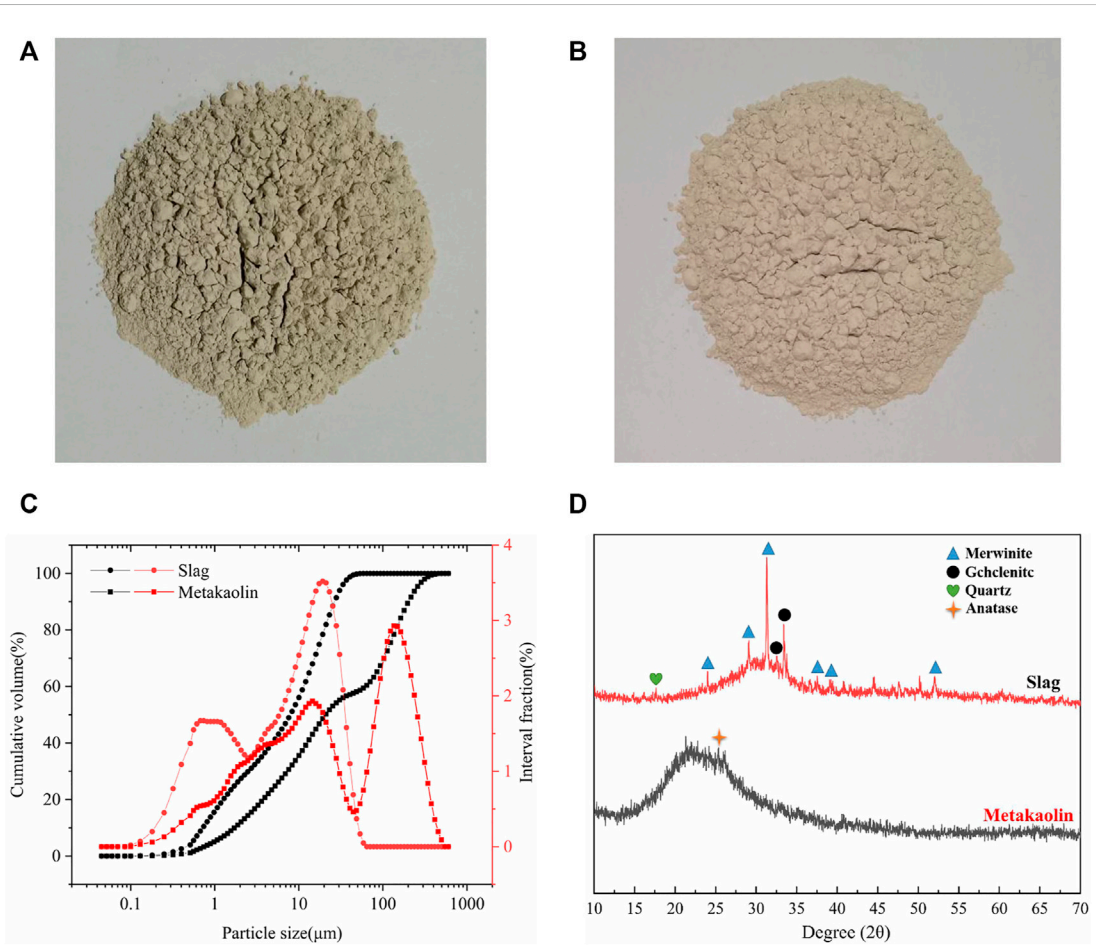


FIGURE 1
Physicochemical properties of raw materials: **(A)** Slag; **(B)** Metakaolin; **(C)** Particle size distributions of slag and metakaolin; and **(D)** XRD results of slag and metakaolin.

estimation (Shervin and Soheil, 2018). Table 2 and Figure 2 show the different encodings and levels of the studied independent variables. In addition, the water/binder ratio (ratio of water in activator to binder) of the AASM was 0.4.

According to Formula (1), the optimal response conditions of the compressive strength and autogenous shrinkage of the AASM were obtained using the optimal predictive quadratic model (Auta and Hameed, 2011).

$$Y = \beta_0 + \sum_{i=1}^{k} \beta_{ii} X_i + \left( \sum_{i=1}^{k} \beta_{ii} X_i \right)^2 + \sum_{i=1}^{k-1} \sum_{j=i+1}^{k} \beta_{ii} X_i X_j + e_i \quad (1)$$

In the formula, $Y$ is the predictive response, $\beta$ is the regression coefficient, $X_i$ and $X_j$ are the influencing factors of the independent variable, $k$ is the number of investigated and optimized factors, and $e_i$ is the random error. Compressive

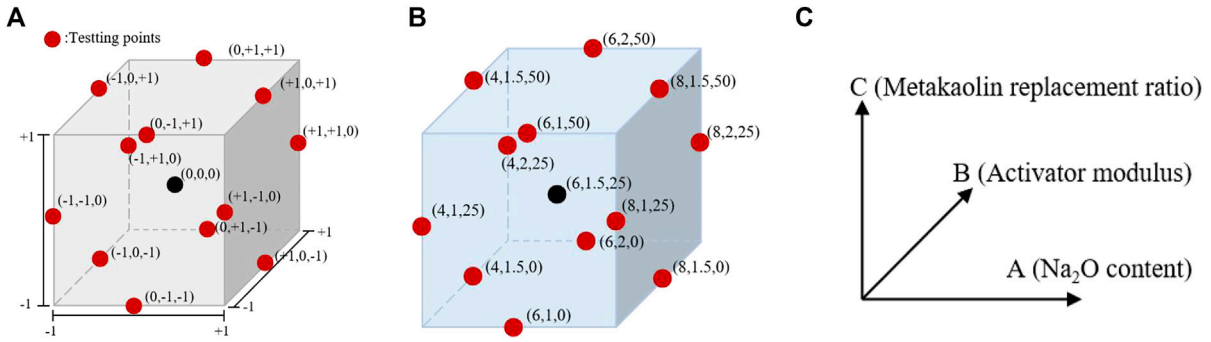


FIGURE 2
Box–Behnken design for three independent variables of prepared geopolymer paste based on **(A)** coding, **(B)** level, and **(C)** coordinate representing the value.

TABLE 2 Response surface factor design and horizontal coding.

| Independent variable factor | Coding and level | | |
|---|---|---|---|
| | −1 | 0 | 1 |
| $Na_2O$ content (A; wt%) | 4 | 6 | 8 |
| Activator modulus (B) | 1.0 | 1.5 | 2.0 |
| Metakaolin replacement ratio (C; wt%) | 0 | 25 | 50 |

strength (at 28 days) and autogenous shrinkage (at 14 days) were used as the response of analysis and statistical interpretation.

## 2.3 Preparation method of specimens

The AASM was tested according to the GB/T 17671-2021 (2021) standard for cement mortar strength testing. First, the sodium silicate solution, solid sodium hydroxide, and deionized water were mixed to prepare alkali activators with $Na_2O$ mass fractions of 4%, 6%, and 8% and activator modulus of 1.0, 1.5, and 2.0, respectively, and aged for 24 h. Metakaolin was mixed with slag according to total binder mass values of 0%, 25%, and 50%, and the mixture was poured into a planetary mixer for premixing to ensure an even mixing of slag and metakaolin. Finally, the activator and standard sand of the corresponding masses were added to the mixer according to a water/binder ratio of 0.4 and a binder/sand ratio of 1:3. The mixed paste was stirred at low speed for 2 min, stirred at high speed for 3 min, and poured into a mold sized 4 cm × 4 cm × 4 cm (length × width × height). Each specimen was vibrated on a vibrating table for 3 min to remove the bubbles in the paste. Then, the specimen was placed in a standard curing box for 24 h (20°C ± 2°C temperature and >90% relative humidity), demolded, and maintained until the preset test age.

## 2.4 Test methods

### 2.4.1 Compressive strength

The strength of the AASM composite paste was tested according to the GB/T 17671-2021 (2021) standard for cement mortar strength testing. The specimens were prepared according to the ratios in Table 3 and the method in Section 2.3. The specimens were cured in a standard curing box until 28 days. The compressive strength of the specimens was tested by a constant-stress pressure test at a loading rate of 2.4 $kNs^{-1}$, and the average compressive strength of three specimens was recorded.

### 2.4.2 Autogenous shrinkage

Autogenous shrinkage was tested using CABR-ZES noncontact bellows in accordance with the ASTM C1698-2009 (2009) testing standard for the autogenous shrinkage of cement paste and mortar. The binder/sand ratio was 1: 3, the inner diameter of the bellows was 29 mm, and the length was 430 mm. The prepared AASM cementitious composite material mortar mixtures were loaded into the bellows. The bubbles in the bellows were eliminated by vibration on the vibrating table, and the bellows were sealed to prevent water loss. Then, the bellows were placed on special support and stored at a constant temperature of 23°C ± 1°C. Shrinkage ($c$) was automatically sampled every 1 min, and the samples were continuously collected over 14 days. The average value of three specimens was recorded as the final result.

Calculation of autogenous shrinkage: After 14 days, the model specimens were removed from the bellows, and the length of each specimen ($L_t$) was measured using an electronic vernier caliper with an accuracy of 0.01 mm. The plastic plug in each bellow was taken out, and its length ($L_s$)

TABLE 3 RSM design and test results of AASM.

| Number | Coded value | | | 28 days compressive strength (MPa) | | 14 days autogenous shrinkage ($\mu m \cdot m^{-1}$) | |
|---|---|---|---|---|---|---|---|
| | A (wt%) | B | C (wt%) | Actual value | Predicted value | Actual value | Predicted value |
| 1 | 6 | 2 | 0 | 80.22 | 77.76 | −2223.25 | −2197.73 |
| 2 | 6 | 1.5 | 25 | 82 | 81.84 | −185.47 | −186.27 |
| 3 | 6 | 1 | 0 | 84.07 | 86.48 | −1665.01 | −1692.26 |
| 4 | 4 | 2 | 25 | 30.2 | 32.59 | −280.31 | −246.74 |
| 5 | 8 | 1 | 25 | 77 | 74.61 | −218.03 | −251.6 |
| 6 | 6 | 1.5 | 25 | 82.4 | 81.84 | −189.47 | −186.27 |
| 7 | 6 | 2 | 50 | 67.28 | 64.87 | −420.59 | −393.33 |
| 8 | 4 | 1 | 25 | 3.26 | 0.7763 | −93.15 | −6.79 |
| 9 | 8 | 1.5 | 50 | 73.15 | 73.08 | −369.05 | −309.95 |
| 10 | 4 | 1.5 | 50 | 5.13 | 5.15 | −35.78 | −96.61 |
| 11 | 6 | 1 | 50 | 24 | 26.46 | −18.17 | −43.69 |
| 12 | 8 | 1.5 | 0 | 98.5 | 98.48 | −2316.34 | −2255.51 |
| 13 | 6 | 1.5 | 25 | 83.4 | 81.84 | −192.47 | −186.27 |
| 14 | 6 | 1.5 | 25 | 80 | 81.84 | −180.47 | −186.27 |
| 15 | 4 | 1.5 | 0 | 52.6 | 52.67 | −1544.92 | −1604.02 |
| 16 | 6 | 1.5 | 25 | 81.4 | 81.84 | −183.47 | −186.27 |
| 17 | 8 | 2 | 25 | 70 | 72.48 | −780.41 | −866.76 |

was measured using the electronic vernier caliper. After 14 days, the slurry length in the bellows was $L = L_t - L_s$, whereas the paste length in the initial bellows was $L_0 = L + c$. The autogenous shrinkage rate is calculated according to Eqs 2, 3.

$$-\triangle L = L - L_0 \tag{2}$$

$$\varepsilon_s = \frac{L - L_0}{L_0} \tag{3}$$

In the formula, $L$ is the length of the mortar in the bellows at time $t$, mm; $L_0$ is the length of the mortar in the initial bellows, mm; $\Delta L$ is the shrinkage value of the mortar at time $t$, mm; and $\varepsilon_s$ is the autogenous shrinkage rate of the mortar at time $t$, $\mu m \cdot m^{-1}$.

### 2.4.3 Microstructural tests

Paste specimens of the cementitious materials were prepared according to Table 3. At the testing age, the paste specimens were crushed, placed in anhydrous ethanol for 3 days to terminate hydration, and placed in a vacuum drying oven for 24 h. Finally, FTIR, SEM, and MIP were performed. A Tensor 27 infrared spectrometer (Bruker, Billerica, MA, US; 4000–400 $cm^{-1}$ test range; 2 $cm^{-1}$ resolution) was used for phase analysis with the sample particle size <74 μm. This particle size was chosen based on other literature (Luo et al., 2022). A Quanta 200 scanning electron microscope (FEI, Hillsboro, OR, US; 5 nm resolution; 20–1×0000 magnification) was used to observe the specimen microstructures period. Before the examination, the dry samples were coated with gold in a vacuum chamber (gold coating in order to make the AASM material has better conductivity). Finally, an Auto Pore IV 9510 automatic Mercury porosimeter (Nocros Corporation, Norcross, Georgia, US; 5 nm–0.34 mm measurement range) was used for pore structure analysis.

## 3 Results and discussion

### 3.1 Regression model analysis

The RSM test results were nonlinearly fitted via the least squares method to obtain regression models of the compressive strength and autogenous shrinkage of the AASM, as shown in Eq. 4, 5.

$$Y_1 = -365.30 + 89.09A + 223.25B - 2.58C - 8.49AB + 0.11AC + 0.94BC - 5.41A^2 - 60.36B^2 - 0.0046C^2 \tag{4}$$

$$Y_2 = -2378.17 + 190.04A + 1088.98B + 81.47C - 93.80AB + 2.19AC + 3.12BC - 17.68A^2 - 343.88B^2 - 1.30C^2 \tag{5}$$

In the formula, $Y_1$ and $Y_2$ are the compressive strength and autogenous shrinkage prediction value, respectively, and $A$, $B$, and $C$ are the $Na_2O$ content, activator modulus, and metakaolin content ratio, respectively. A positive (negative) coefficient

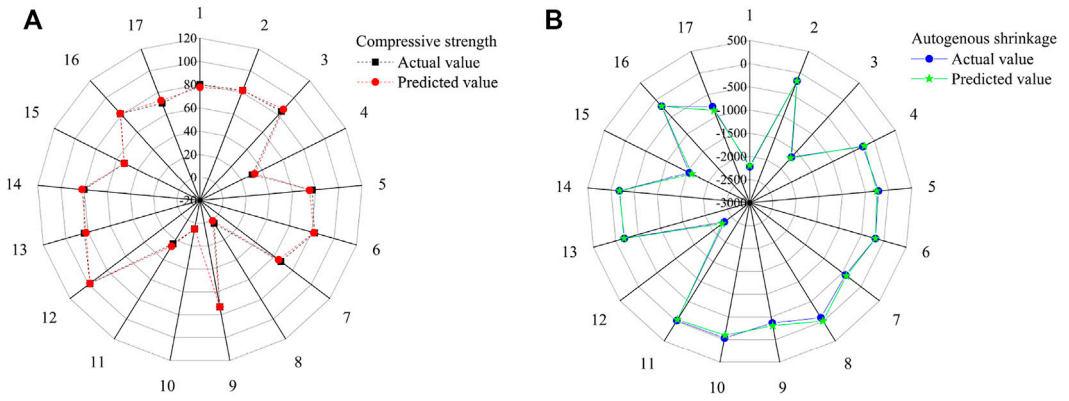


FIGURE 3
Experimental and predicted results of AASM cementitious composite specimens. **(A)** Compressive strength and **(B)** Autogenous shrinkage.

indicates that a positive (negative) change in the independent variable influence factor causes an increase (decrease) in the response value.

### 3.1.1 ANOVA

Figure 3 and Table 3 show the experimental and predicted values of the response surface design for the compressive strength and autogenous shrinkage of the AASM. The results predicted by the model almost coincide with the measured values. For further evaluation of model accuracy and reliability, ANOVA was performed to conduct an explicit model test, and the results are shown in Table 4. The significance of independent variable influencing factors in a regression model for the predicted value of response is generally evaluated using the $p$ value (Zhang et al., 2017; Lin et al., 2018); $p < 0.0001$ indicates a highly significant impact, $p < 0.05$ denotes significant impact, and $p > 0.05$ suggests that the impact is not significant. According to Table 4, the compressive strength of the 28 days specimen and the $p$ value of the autogenous shrinkage model of the 14 days specimen are is than 0.0001, indicating that the model is highly significant and reliable.

### 3.1.2 ANOVA and significance test of response surface model

The statistical analysis of model fitting accuracy is shown in Table 4. According to Table 4, the complex correlation coefficient ($R^2$) of the compressive strength model is 0.9961, the corrected correlation coefficient ($R_{Adj}{}^2$) is 0.9911, and the predicted correlation coefficient ($R_{pred}{}^2$) is 0.9441, indicating that 99.11% of the change in the compressive strength response value can be explained by this model. The complex correlation coefficient ($R^2$) of the autogenous shrinkage model is 0.9965, the corrected correlation coefficient ($R_{Adj}{}^2$) is 0.9919, and the predicted correlation coefficient ($R_{pred}{}^2$) is 0.9434, indicating that 99.65% of the change in the autogenous shrinkage response value can be explained by this model. Overall, the compressive strength and autogenous shrinkage model have high accuracy.

The experimental and predicted values of the compressive strength and autogenous shrinkage model are compared in Figure 4. The experimental values are evenly scattered along the $y = x$ line and on both sides of the line. The experimental and predicted values show good consistency. The model fit is high, and the fitting effect is good. In summary, the quadratic polynomial model can be used to analyze and optimize the compressive strength and autogenous shrinkage of the AASM, thereby providing a theoretical basis for the composition design of such materials.

## 3.2 Three-dimensional response surface interaction analysis

A three-dimensional response surface can intuitively describe the relationship between the interaction of two factors and a response value, thus summarizing the influence law of the change in the factor level on the response value. The greater the curvature of the response surface, the more significant the interaction of factors. However, this suggests that the influence of factors is not evident (Lao et al., 2018). A three-dimensional response surface diagram was constructed with each factor level as the X- and $Y$-axis coordinates and the compressive strength and autogenous shrinkage as the $Z$-axis coordinate. The response surface shape and contour explain the strength of interaction between factors. The steeper the response surface, the more elliptical the contour and the more evident the interaction between factors. The smoother the response

10.3389/fbuil.2022.1020217

TABLE 4 ANOVA of response surface regression model.

| Compressive strength | Source | Sum of square | DF | Mean square | *F* Value | *p* Value | Significance |
|---|---|---|---|---|---|---|---|
| | Model | 13716.33 | 9 | 1524.04 | 198.08 | <0.0001 | Significant |
| | A | 6467.26 | 1 | 6467.26 | 840.57 | <0.0001 | — |
| | B | 440.6 | 1 | 440.6 | 57.27 | 0.0001 | — |
| | C | 2658.3 | 1 | 2658.3 | 345.51 | <0.0001 | — |
| | AB | 287.98 | 1 | 287.98 | 37.43 | 0.0005 | — |
| | AC | 122.32 | 1 | 122.32 | 15.9 | 0.0053 | — |
| | BC | 555.31 | 1 | 555.31 | 72.18 | <0.0001 | — |
| | $A^2$ | 1971.06 | 1 | 1971.06 | 256.19 | <0.0001 | — |
| | $B^2$ | 958.61 | 1 | 958.61 | 124.59 | <0.0001 | — |
| | $C^2$ | 34.41 | 1 | 34.41 | 4.47 | 0.0723 | — |
| | Residual | 53.86 | 7 | 7.69 | — | — | — |
| | Lack of fit | 47.51 | 3 | 15.84 | 9.97 | 0.025 | Significant |
| | Pure error | 6.35 | 4 | 1.59 | — | — | — |
| Cor total | 13770.18 | 16 | — | — | — | — | |
| $R^2$ = 0.9961 | | $R_{Adj}^2$ = 0.9911 | | $R_{Pred}^2$ = 0.9441 | | $C_V$ = 4.39% | |
| Autogenous shrinkage | Source | Sum of square | DF | Mean square | *F* value | *p* value | Significance |
| | Model | $9.68\times10^6$ | 9 | $1.08\times10^6$ | 218.66 | <0.0001 | Significant |
| | A | $3.74\times10^5$ | 1 | $3.74\times10^5$ | 76.02 | <0.0001 | — |
| | B | $3.66\times10^5$ | 1 | $3.66\times10^5$ | 74.32 | <0.0001 | — |
| | C | $5.96\times10^6$ | 1 | $5.96\times10^6$ | 1211.89 | <0.0001 | — |
| | AB | 35195.46 | 1 | 35195.46 | 7.15 | 0.0318 | — |
| | AC | 47992.95 | 1 | 47992.95 | 9.76 | 0.0168 | — |
| | BC | 6069.96 | 1 | 6069.96 | 1.23 | 0.3033 | — |
| | $A^2$ | 21067.92 | 1 | 21067.92 | 4.28 | 0.0773 | — |
| | $B^2$ | 31118.45 | 1 | 31118.45 | 6.33 | 0.0401 | — |
| | $C^2$ | $2.76\times10^6$ | 1 | $2.76\times10^6$ | 560.91 | <0.0001 | — |
| | Residual | 34434.15 | 7 | 4919.16 | — | — | — |
| | Lack of fit | 34343.35 | 3 | 11447.78 | 504.31 | <0.0001 | Significant |
| | Pure error | 90.8 | 4 | 22.7 | — | — | — |
| | Cor total | $9.72\times10^6$ | 16 | — | — | — | — |
| $R^2$ = 0.9965 | | $R_{Adj}^2$ = 0.9919 | | $R_{Pred}^2$ = 0.9434 | | $C_V$ = 9.94% | |

Notes: DF, degree freedom; *F* value, ratio of the mean square to the residual term; *p* value, influence degree value of each factor; $R^2$, complex correlation coefficient; $R_{Adj}^2$, correction correlation coefficient; $R_{Pred}^2$, predictive correlation coefficient; $C_V$, coefficient of variation.

surface, the more circular the contour and the less obvious the interaction between factors. The more numerous the contour lines distributed on the coordinate axis, the more noticeable the influence of factors.

### 3.2.1 Interaction analysis of compressive strength

Figure 5A is the compressive strength response surface diagram of the AASM under the interaction of $Na_2O$ content and activator modulus at a metakaolin content of 25%, and Figure 5B is the contour map corresponding to the response surface. According to Figure 5A, when the modulus is 1.0–2.0, the compressive strength increases with $Na_2O$ content. When the modulus is 1.0 and $Na_2O$ content increases from 4% to 8%, the compressive strength of the AASM increases from 3.26 to 77 MPa (an increase of 2261.96%). Hence, $Na^+$ and $OH^-$ are the main forces driving the rise in compressive strength. When the $Na_2O$ content is 4%–8% and the activator modulus increases from 1.0 to 2.0, the compressive strength of the AASM increases and then decreases with the modulus. Thus, the modulus of the activator can promote the development of the compressive strength of the materials to a certain extent. In Figure 5B contour map, the interaction between $Na_2O$ content and activator modulus is more evident. The reason is that a high $Na_2O$ content is beneficial to the dissolution of a solid precursor, and a high modulus can quickly provide a large number of silicates, thus accelerating the hydration reaction of a composite system. However, a high modulus will cause the hydration products generated by the rapid reaction to cover the unreacted solid precursor, thereby reducing the hydration

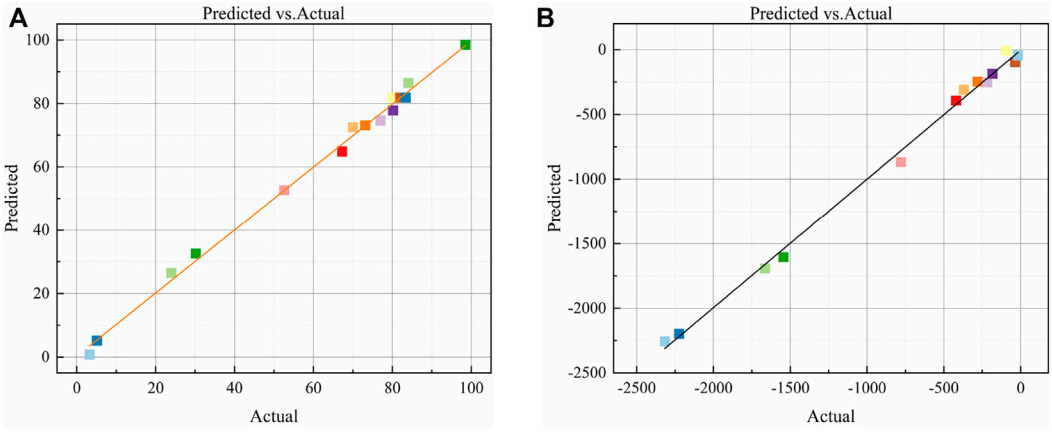


FIGURE 4
Comparative analysis of predicted and experimental values of AASM. **(A)** Compressive strength and **(B)** Autogenous shrinkage.

products and compressive strength. Therefore, a high $Na_2O$ content is conducive to the better functioning of modulus factors. Moreover, a certain range of the modulus can promote the $Na_2O$ content factor. In their interaction process, the contour lines are more distributed in the abscissa than in the ordinate (Figure 5B), indicating that the effect of the $Na_2O$ content on the compressive strength of the cementitious composite materials is greater than that of the activator modulus. With an increase in $Na_2O$ content, the compressive strength of the AASM increases, which is consistent with the results of Zhan et al. (2022) and Ma Qianmin et al. (Ma et al., 2019). This is due to the preparation of cementitious materials; if the $Na_2O$ content is small, the slag–metakaolin monomer is in the low-alkalinity environment, and the monomer dissolution rate is low (Rynel, 2015), then a slow hydration reaction of cementitious materials will decrease the compressive strength. With an increase in alkali content, the monomer dissolution rates of the slag and metakaolin solid precursors increase, monomer collision quickly generates C-A-S-H and N-A-S-H gels, and compressive strength increases. However, Shengtu et al. (2019) found that with a rise in alkali content, the compressive strength of geopolymers increased and then decreased, and the reason may be related to the types of raw materials.

Figures 5C,D depict the effect of the interaction between metakaolin content and $Na_2O$ content on the compressive strength of the AASM when the modulus of the activator is 1.5. As seen in Figure 5C, compressive strength decreases with an increase in metakaolin content but increases with an increase in $Na_2O$ content. When the $Na_2O$ content is 4% and the metakaolin content increases from 0% to 50%, the compressive strength of the AASM decreases from 84.1 to 24 MPa (reduced by 71.46%). When the metakaolin content is 50% and the $Na_2O$ content increases from 4% to 8%, the compressive strength increases from 5.13 to 73.15 MPa (increased by 1325.93%). These results show that a high alkali content is beneficial to the dissolution of solid precursors. C-A-S-H and N-A-S-H gels are rapidly generated by the collision between dissolved monomers, which improves the compressive strength of the AASM. However, high content of metakaolin is not conducive to the development of the compressive strength of AASM. In the presence of both metakaolin and slag, under the action of an alkaline activator, slag dissolves before metakaolin. During the reaction, slag consumes a large amount of $OH^-$, and the alkaline solution concentration decreases. With an increase in metakaolin content, the depolymerization ability of the low-alkalinity solution on aluminosilicate minerals decreases. At this time, N-A-S-H gel is the main hydration product, and the amount of C-A-S-H gel is small, resulting in a decrease in the compressive strength of the system (Zhan et al., 2022). As illustrated in Figure 5D, when the metakaolin content and $Na_2O$ content interact, the contour distribution in the abscissa is wider than that in the ordinate, indicating that the influence of $Na_2O$ content on compressive strength is greater than that of metakaolin content.

Figures 5E,F show the effects of the interaction between the modulus of the activator and the metakaolin content on compressive strength. The compressive strength of the AASM increases and then decreases with an increase in the modulus of the activator and decreases with an increase in the metakaolin content. This indicates the existence of an optimal activator modulus, which maximizes the compressive strength of the AASM. Furthermore, high content of metakaolin has an inhibitory effect on compressive strength. This is because a large modulus quickly generates a large quantity of $SiO_3^{2-}$ for the system. Despite the considerable amounts of $SiO_3^{2-}$ and metakaolin, the slag hydrolysis of $Ca^{2+}$, $Si^{4+}$, and $Al^{3+}$ reacts to form C-S-H, C-A-S-H, and N-A-S-H gels. Ca/Si changes in the molding process and the possible existence of free silica gel easily

10.3389/fbuil.2022.1020217

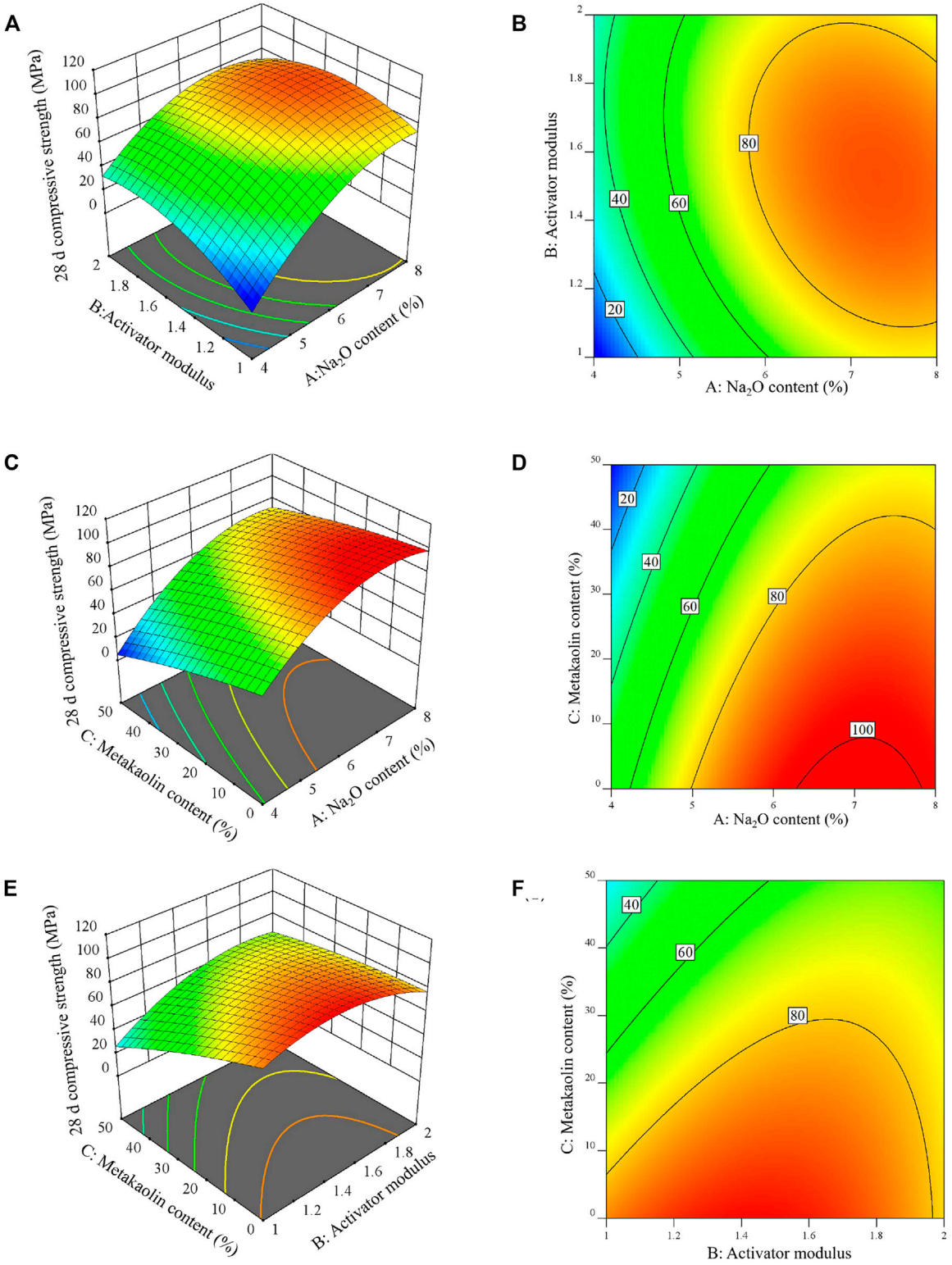


FIGURE 5
3D response surface diagrams of compressive strength of AASM.

10.3389/fbuil.2022.1020217

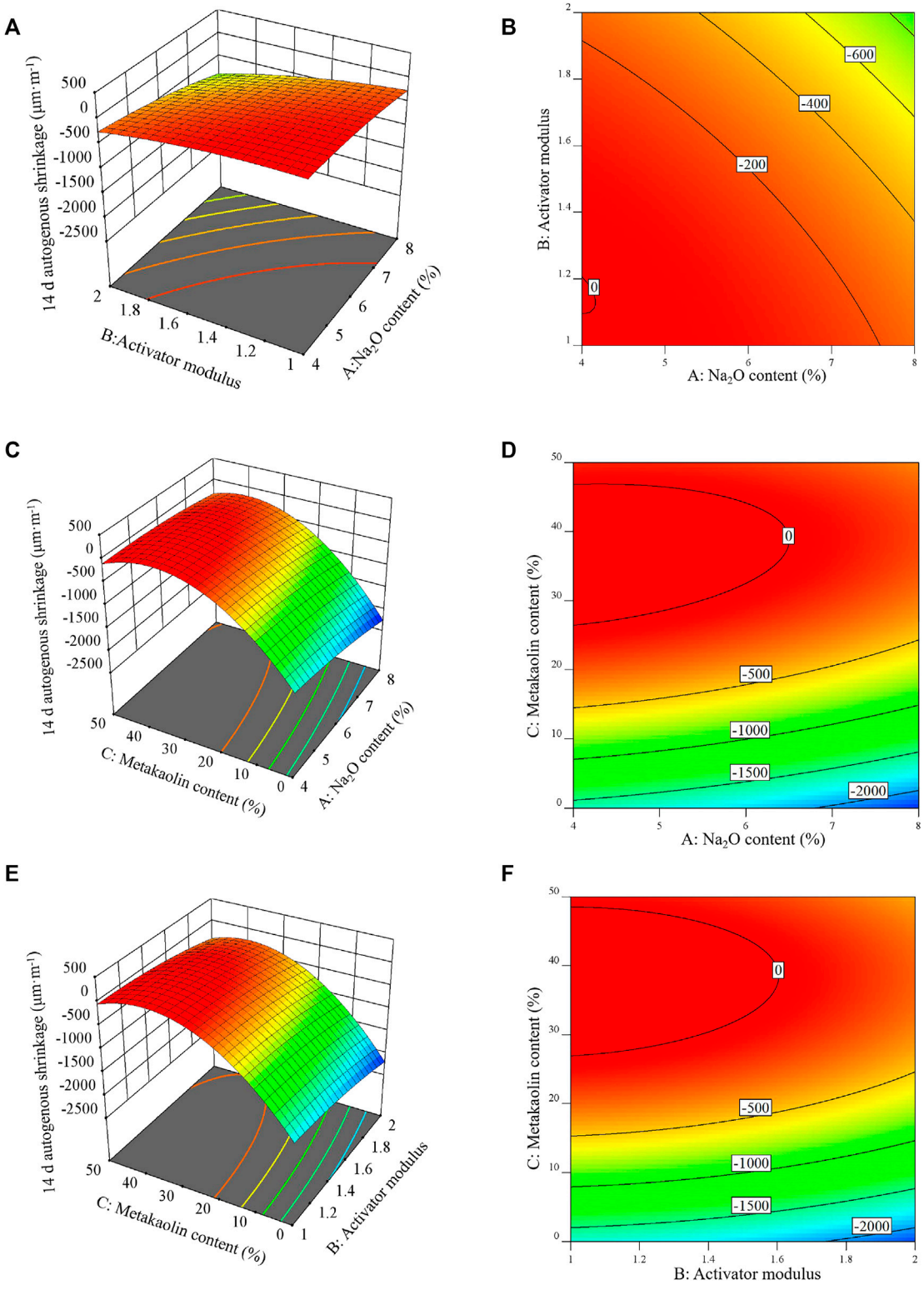


FIGURE 6
3D response surface diagrams of autogenous shrinkage of AASM.

lead to internal defects in the cementitious material system, resulting in a decrease in compressive strength. In addition, the higher the modulus, the lower the alkalinity of the solution; metakaolin and slag activity cannot be effectively stimulated (Duxson et al., 2005). As the high metakaolin content further increases, the large quantities of $Si^{4+}$ and $Al^{3+}$ dissolved in metakaolin react with $SiO_3^{2-}$, hence increasing the generated N-A-S-H and reducing system strength (Chen, 2018). As shown by the contour map in Figure 5F, when the modulus of the activator and metakaolin content interact, the contour distribution in the ordinate is wider than that in the abscissa, indicating that the effect of metakaolin content on the compressive strength of the AASM is greater than that of the activator modulus.

ANOVA and response surface analysis findings imply that $Na_2O$ content evidently affects the compressive strength of the AASM as a single factor. The significance of the effects of the factor interactions on the AASM is in the following order: activator modulus and metakaolin content > $Na_2O$ content and activator modulus > $Na_2O$ content and metakaolin content. This is because, in a certain range of the modulus, the $SiO_3^{2-}$ in the solution is conducive to the acceleration of the hydration reaction of the slag–metakaolin composite system, increase in the reaction products and enhancement in the compressive strength of the AASM composite system.

### 3.2.2 Autogenous shrinkage

The autogenous shrinkage response surface diagram and contour map of the AASM under the interaction of $Na_2O$ content and activator modulus at 25% metakaolin content are shown in Figures 6A,B. As seen in Figure 6A, when the modulus is 1.0 and the $Na_2O$ content increases from 4% to 8%, the autogenous shrinkage (absolute value) of the AASM increases from 93.15 to 218.03 μm $m^{-1}$ (increased by 134.06%). When the modulus is 2.0, and the $Na_2O$ content increases from 4% to 8%, autogenous shrinkage (absolute value) increases from 280.31 to 780.41 μm $m^{-1}$ (increased by 178.41%). In summary, the autogenous shrinkage of the AASM composite increases with $Na_2O$ content and activator modulus. The reason is that in an environment with a high alkali content and high activator modulus, the $OH^-$ and $[SiO_4]^{4-}$ ion concentrations in the alkaline solution increase, and the metakaolin and slag particles rapidly react with the $OH^-$ and $[SiO_4]^{4-}$ plasma, and the water in the system is consumed quickly to form a gel network system, resulting in capillary pressure and increasing autogenous shrinkage (Li et al., 2021). The contour lines in Figure 6B are nearly parallel, indicating that the autogenous shrinkage effect of $Na_2O$ content and activator modulus on the AASM is not obvious. Furthermore, within the variable range of $Na_2O$ content and activator modulus, the autogenous shrinkage change of the AASM is small, which may be due to the large $Na_2O$ content, high solution pH, and strong alkalinity. The larger the modulus of the activator, the lower the pH of the solution and the weaker the alkalinity. When the $Na_2O$ dosage and activator modulus increase simultaneously, the alkaline solution compensates for each other such that their interaction effect is not obvious.

Figures 6C,D reflect the effect of the interaction between metakaolin content and $Na_2O$ content on the compressive strength of the AASM when the modulus of the activator is 1.5. As shown by Figure 6C, when the $Na_2O$ content is between 4% and 8%, the autogenous shrinkage of the AASM decreases with an increase in metakaolin content. The autogenous shrinkage value increases with $Na_2O$ content. For example, with 4% $Na_2O$ content, the metakaolin content increases from 0% to 50%, and the autogenous shrinkage value decreases from 1544.92 to 35.78 μm $m^{-1}$ (reduced by 97.68%). When the metakaolin content is 50% and the $Na_2O$ content increases from 4% to 8%, the autogenous shrinkage of the AASM increases from 35.78 to 369.05 μm $m^{-1}$ (increased by 931.44%). Under the interaction of metakaolin and $Na_2O$ contents, $Na_2O$ (metakaolin) content increases (decreases) the autogenous shrinkage of the AASM. Because of the rising metakaolin content, metakaolin reacts to produce a gel product with a zeolite-like structure under the action of the alkali solution, which improves the uniformity of the system structure and enhances the autogenous shrinkage of the AASM (Li et al., 2021). However, Yang et al. (2017) found that with an increase in curing age, metakaolin geopolymers expanded and then shrunk, and a higher metakaolin content led to a longer expansion time. Palumbo et al. (2018) and Antonio et al. (2008) also found early expansion. The reason for the expansion may be related to the zeolite-like structure (i.e., three-dimensional network structure) generated by the hydration reaction of metakaolin. Figure 6D contour map shows that the interaction between metakaolin content and $Na_2O$ content is more evident, and the effect of metakaolin content on autogenous shrinkage is greater than that of $Na_2O$ content.

Figures 6E,F show the effect of the interaction between the modulus of the activator and metakaolin content on the autogenous shrinkage response surface of the AASM. As illustrated in Figure 6E, autogenous shrinkage increases with the modulus but decreases with an increase in metakaolin content. The reason is that the larger the modulus, the more abundant the active $[SiO_4]^{4-}$ groups in the activator solution. Metakaolin and slag particles dissolve rapidly under the catalysis of $OH^-$, thus releasing $Ca^{2+}$, $A1^{3+}$, and $Si^{4+}$ plasma to react with many $[SiO_4]^{4-}$ groups and then produce more C-A-S-H gel; this C-A-S-H gel shrinks considerably, resulting in greater autogenous shrinkage of the composite system (Chen et al., 2014; Liao et al., 2017; Yang, 2020). As the metakaolin content increases, N-A-S-H formation is enhanced, and the C-A-S-H gel is reduced, so system shrinkage is mitigated. However, Wang (2018) found that with an increase in the activator modulus, the autogenous shrinkage of cementitious composite materials decreased, which may be related to the types

of raw materials. The contour map in Figure 6F shows that the interaction between metakaolin content and activator modulus is highly obvious, and the effect of metakaolin content on autogenous shrinkage is greater than that of the activator modulus.

ANOVA and response surface analysis results indicate that metakaolin content is an obvious single factor affecting the autogenous shrinkage of the AASM. The significance of the effects of the factor interactions on autogenous shrinkage is in the following order: $Na_2O$ content and metakaolin content > $Na_2O$ content and activator modulus > activator modulus and metakaolin content. The reason is that a high $Na_2O$ content is beneficial to the dissolution of a solid precursor, thereby accelerating the hydration reaction of cementitious materials. This results in gel precipitation in a very early stage, which slows the subsequent hydration reaction, thereby enhancing the pore size, porosity, and autogenous shrinkage of the composite system. A high metakaolin content provides large amounts of $A1^{3+}$ and $Si^{4+}$ for the system, which makes the reaction generate more N-A-S-H and reduces autogenous shrinkage. Therefore, under the action of a high alkali $Na_2O$ content, metakaolin plays a larger role. On the contrary, autogenous shrinkage is reduced under a high metakaolin content. In general, the two factors share a complementary relationship in their interaction process.

## 3.3 Microscopic analysis

ANOVA and response surface analysis results (Section 3.1 and Section 3.2) show that the $Na_2O$ and metakaolin contents are the significant factors affecting the compressive strength and autogenous shrinkage of the AASM. In addition, the interactions between $Na_2O$ and metakaolin and between the sodium silicate modulus and metakaolin are the significant factors affecting compressive strength and autogenous shrinkage, respectively. Five groups of samples (fifth, ninth, 10th, 12th, and 17th) were selected to study the effects of $Na_2O$ content, sodium silicate modulus, metakaolin content, and their interactions on the phase compositions, microstructures, and porosity of the AASM.

### 3.3.1 FTIR analysis

FTIR spectra of the selected samples were obtained to describe the effect of the interactions among $Na_2O$ content, metakaolin content, and water glass modulus on the phase compositions of the AASM, and the results are shown in Figure 7. The findings from test pieces 5, 9, 10, and 17 suggest that during the interaction of the $Na_2O$ content and the activator modulus, more $Na_2O$ is generated, and the Si–O–Si vibration peaks at approximately 455–456 and 870 $cm^{-1}$ move toward low wave numbers. Therefore, the substitution rate of Al for Si is higher in a highly alkaline environment; that is, the reaction level of the AASM is higher, which proves that a highly

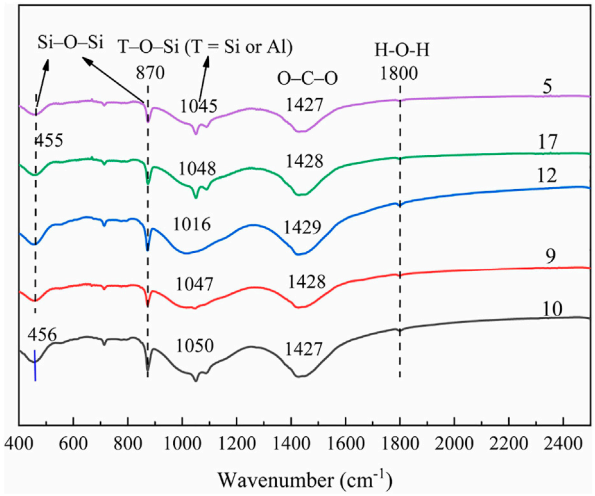


FIGURE 7
FTIR spectra of AASM.

alkaline environment is conducive to the reaction of metakaolin and slag. This is consistent with Zhan et al. (2022). The vibration peak at 1047–1050 $cm^{-1}$ represents the vibration of the *T*–O–Si (where *T* is Si or Al) asymmetric functional group. With an increase in $Na_2O$ content from 4% to 8%, the wave number of this band decreases from 1050 to 1047 $cm^{-1}$. This is because the incorporation of $Na_2O$ significantly promotes the reaction of the AASM. The reaction products (N-A-S-H and C-A-S-H gels) increase, and the strength of the AASM increases. The vibration peak at 1427–1428 $cm^{-1}$, which represents the stretching vibration of O–C–O, gradually increases with an increase in $Na_2O$ content owing to the reaction of the alkaline activator on the sample surface with carbonate in the atmosphere (Bernal et al., 2011; Wan et al., 2017). The band near 1800 $cm^{-1}$ is due to the stretching vibration of hydroxyl (–OH) in the Si–OH or Al–OH functional groups and due to the H–O–H stretching vibration caused by water changes in the AASM. With an increase in the excitation modulus, the asymmetric stretching of Si–O–T shifts to a higher wave number. This is because more silicates are introduced into the system to form a silicon-rich gel phase (Bernal et al., 2011). In addition, compared with that in the $Na_2O$ content, an increase in the activator modulus can directly add more silicates into the system, thereby reducing the Ca/Si and Al/Si ratios in the gel and promoting the formation of a high-level silicon-rich gel phase. As the modulus of the activator increases, the band expands at approximately 1045–1048 $cm^{-1}$, and the asymmetric stretching vibration intensity of the bond increases at approximately 455 $cm^{-1}$. As for the interaction between the $Na_2O$ content and activator modulus, a highly alkaline environment is conducive to the dissolution of the solid precursors $Ca^{2+}$, $A1^{3+}$, and $Si^{4+}$. Furthermore, a high modulus provides large amounts of $[SiO_4]^{4-}$, $Ca^{2+}$, $A1^{3+}$, and

$Si^{4+}$ and $[SiO_4]^{4-}$ reaction. Consequently, the system hydration reaction is accelerated, and the hydration products increase. Therefore, the activator modulus plays a better role under the action of high $Na_2O$ content, and the $Na_2O$ content factor is promoted under the condition of a high modulus. This is consistent with Pu's conclusion. (Pu, 2010).

Specimens 9, 10, and 12 show the effect of the interaction between the $Na_2O$ and metakaolin contents on the phase transition of the AASM. The main absorption peak emerges at 1016–1050 $cm^{-1}$ owing to the uneven vibration of the Si–O–*T* (where *T* is Si or Al) bond. When metakaolin content increases from 0% to 50%, the wave number of this band increases from 1016 to 1050 $cm^{-1}$. This is because more $Al^{3+}$ in metakaolin is involved in the reaction, resulting in the formation of C-A-S-H gel with a high degree of polymerization. Moreover, the higher the metakaolin content, the weaker the strength of the band. This suggests that the quantity of the reaction products of the AASM is reduced, thereby decreasing compressive strength and autogenous shrinkage. At 455–456 and 870 $cm^{-1}$, owing to the bending vibration of the Al–O–Si bond, the band intensities of specimens 10 and 12 are proportional to the metakaolin content, which may be related to the introduction of additional $Al^{3+}$ and $Si^{4+}$ (Wan et al., 2017). In the interaction of the $Na_2O$ and metakaolin contents, the greater the $Na_2O$ content, the more abundant the $OH^-$ and $Na^+$ in the solution; the higher the metakaolin content, the larger the amount of added $A1^{3+}$ and $Si^{4+}$, and the vibration of the *T*–O–Si (where *T* is Si or Al) asymmetric functional group moves to a high-wave-number range. At this time, $OH^-$ and $Na^+$ react with $Al^{3+}$ and $Si^{4+}$ in the solution; this forms a larger quantity of N-A-S-H, thereby reducing compressive strength and autogenous shrinkage.

As seen from the results of specimens 5, 9, 12, and 17, when the sodium silicate modulus and metakaolin content interact, the larger the modulus, the greater the number of active $[SiO_4]^{4-}$ groups in the activator solution, and the asymmetric stretching of the Si–O–*T* bond shifts to higher wave numbers. More $SiO_3^{2-}$ reacts with metakaolin and slag-hydrolyzed $Ca^{2+}$, $Si^{4+}$, and $Al^{3+}$ to form C-S-H, C-A-S-H, and N-A-S-H gels, which makes the structure of the AASM denser. Consequently, the number of pores increases and the capillary stress produced by meniscus formation is enhanced, resulting in greater autogenous shrinkage of the composite system. These findings contradict those of Wang Dongping (Wan et al., 2017), possibly because of the use of different raw materials.

### 3.3.2 SEM analysis

Figures 8A–C show the micromorphologies under the interactions of $Na_2O$ content and water glass modulus, $Na_2O$ content and metakaolin, and water glass modulus and metakaolin, respectively. As depicted in Figure 8A, the microstructure of the AASM is relatively dense, but there are also large microcracks. Therefore, when $Na_2O$ is combined with the modulus of the activator, the two properties can complement each other. The reason is that a high $Na_2O$ content is beneficial to the dissolution of solid precursors. However, in a high-$Na_2O$ environment, the internal microcracks of the AASM cementitious composite material system increase and shrink. The high modulus provides a large number of silicates for the system, which accelerates its hydration reaction. However, the higher the modulus, the weaker the basicity of the solution and the alkali solution cannot effectively stimulate the solid precursor. Thus, the hydration products and compressive strength decrease. Therefore, under the interaction between $Na_2O$ content and activator modulus, the modulus effect is better under the action of high $Na_2O$ content, whereas the $Na_2O$ content factor is promoted under a high modulus. The interaction between $Na_2O$ content and activator modulus is highly conducive to the development of the mechanical properties of the AASM and increases their volume stability.

Response surface analysis shows that the interaction between $Na_2O$ and metakaolin contents exerts the most significant effect on the autogenous shrinkage of the AASM. According to Figure 8B, under the interaction of $Na_2O$ and metakaolin contents, unreacted slag and many microcracks are seen in the micromorphology. This is because, in the presence of both $Na_2O$ and metakaolin, metakaolin consumes more $OH^-$, thereby reducing the pH of the system. In this case, the alkaline environment cannot stimulate the solid precursor, resulting in the presence of some unreacted slag. With an increase in metakaolin content, the hydration products (N-A-S-H) increase, but the hydration products in the system are mainly C-A-S-H. The greater the amount of C-A-S-H gel, the more abundant the cracks in the system and the larger the shrinkage of the system. Such an increase in metakaolin content can reduce the formation of cracks and alleviate autogenous shrinkage. Therefore, under the interaction of $Na_2O$ and metakaolin contents, the structural density of the composite system increases, and the microcrack width decreases.

Moreover, the response surface analysis results indicate that the interaction between the activator modulus and metakaolin content has the most significant effect on the compressive strength of the AASM. As seen in Figure 8C, the cementitious composite materials have a dense microstructure, a relatively smooth surface structure, and some fine cracks. This is because in the presence of both the modulus of the activator and metakaolin content, the high modulus provides a large amount of $SiO_3^{2-}$ for the system. $SiO_3^{2-}$ reacts with metakaolin and the $Ca^{2+}$, $Si^{4+}$, and $Al^{3+}$ hydrolyzed by slag to form C-S-H, C-A-S-H, and N-A-S-H gels. With an increase in metakaolin content, the N-A-S-H generated by the system increases. The N-A-S-H and C-A-S-H gels are filled with each other, so the system structure becomes more compact, and the microcracks are reduced. Similarly, the incorporation of metakaolin exerts a certain filling effect; metakaolin is incorporated, and metakaolin and slag are doped with each other. The close accumulation of large and

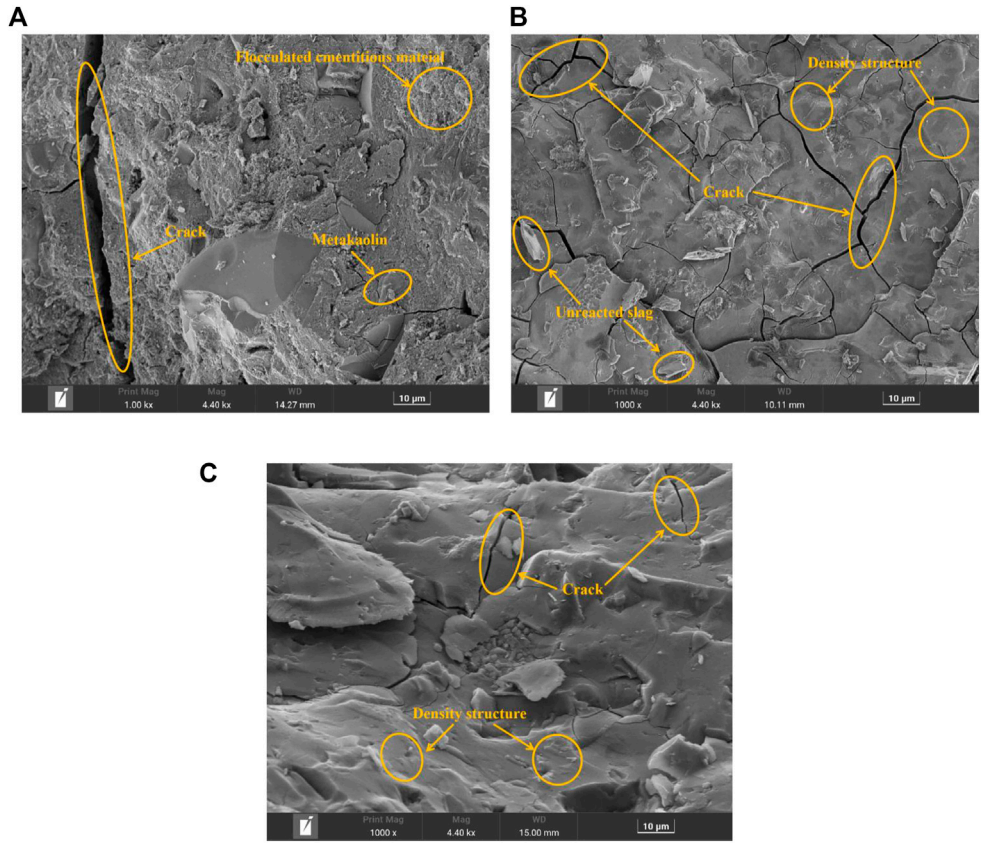


FIGURE 8
Micromorphologies of AASM. **(A)** Interaction between $Na_2O$ and activator modulus; **(B)** Interaction between $Na_2O$ and metakaolin; and **(C)** Interaction between activator modulus and metakaolin.

small particles reduces the size and number of macropores, which refines and scales down the pores of the AASM, increases the density of the hardened body structure, reduces crack generation, and improves the volume stability of the cementitious composite materials. This is consistent with Cui et al. (2017).

### 3.3.3 MIP analysis

MIP was conducted to further explain the influence of the interactions of $Na_2O$ content, activator modulus, and metakaolin content on the pore structure of the AASM. The pore volume distribution and pore size distribution are shown in Figure 9. Pores are divided into the following categories: gel pores (<10 nm), transition pores (10–100 nm), pores (100–1000 nm), and macropores (>1000 nm) (Guo, 2004). According to the findings from test pieces 5, 9, 10, and 17 in Figure 9A, under the interaction of $Na_2O$ content and activator modulus, the larger the $Na_2O$ content, the smaller the cumulative pore volume and porosity of the AASM. When the modulus is 1.5 and the $Na_2O$ content increases from 4% to 8%, porosity decreases from 11.01% to 10.02% (reduced by 9%). Such an increase in $Na_2O$ content reduces the total pore volume because highly alkaline solutions can promote the dissolution and decomposition of metakaolin and slag particles; the reaction degree of cementitious materials also improves, resulting in the coarsening and reduction of gel pores, increase in capillaries, rise in capillary tension, and shrinkage of AASM. When the $Na_2O$ content is 8% and the activator modulus increases from 1.0 to 2.0, porosity increases from 26.20% to 30.13% (increased by 15%). That is, the total pore volume of the AASM increases with the activator modulus. The reason is that an increase in the activator modulus introduces more soluble silica into the system, which increases mixture viscosity and porosity (Nedeljkovi, 2019). The curves of specimens 5 and 17 have a consistent trend, indicating that the modulus of sodium silicate does not affect pore uniformity and has little effect on the change in pore size distribution. The above analysis suggests that under the interaction of $Na_2O$ content and water glass modulus, their properties can complement each other, as both are activators. Therefore, this interaction has little effect on the AASM.

According to the results of specimens 9, 10, and 12 in Figures 9A,B, under the interaction between $Na_2O$ and

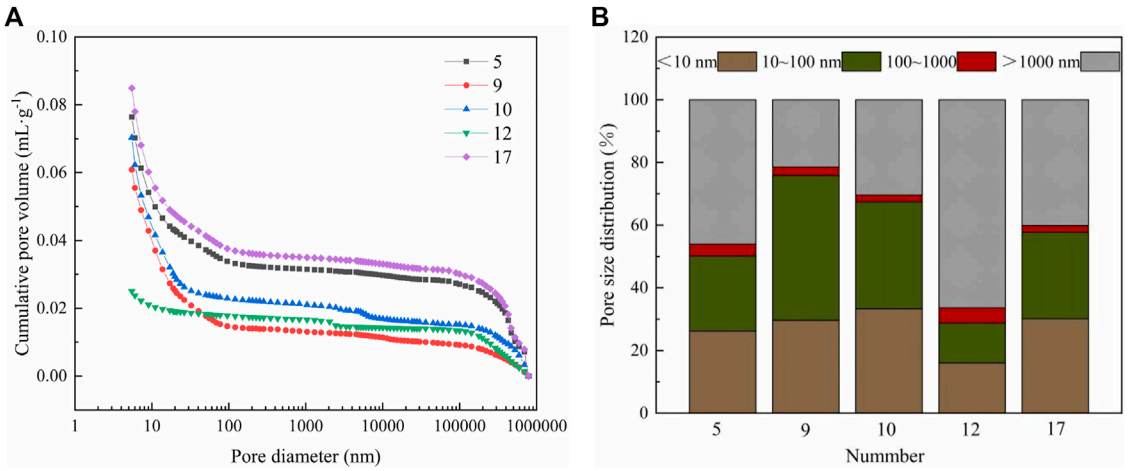


FIGURE 9
MIP spectra of AASM. **(A)** Cumulative pore volume and **(B)** Pore size distribution.

metakaolin contents, porosity increases with metakaolin content. With 8% $Na_2O$ content and an increase in metakaolin content from 0% to 50%, porosity increases by 141.98%. Such an increase in metakaolin content leads to an increase in the porosity of the cementitious materials. This result is consistent with those of Nedeljkovi (2019) and Zhang et al. (2016). With increasing metakaolin content, the gel pores (<10 nm) and transition pores (10–100 nm) of the AASM increase during the macropores (>1000 nm) decrease. As stated by Hansen (1987), the more numerous the capillary pores, the greater the paste shrinkage. However, according to a previous report (Paulo et al., 2016), the increased metakaolin content helps improve the pore size distribution and reduce the autogenous shrinkage of the specimens. Combined with the FTIR analysis results, this discussion implies that when $Na_2O$ interacts with metakaolin, $Na_2O$ promotes the dissolution of metakaolin, and metakaolin provides large amounts of $A1^{3+}$ and $Si^{4+}$. $OH^-$ and $Na^+$ react with $A1^{3+}$ and $Si^{4+}$ in the solution, and the proportion of the formed hydration product (N-A-S-H) increases, thus significantly reducing the structural compactness of the AASM; this decreases the compressive strength but coarsens the pore structure and increases volume stability (Li et al., 2017b; Ren et al., 2022b).

From specimens 5, 9, 12, and 17 in Figures 9A,B, under the interaction of the activator modulus and metakaolin content, they reduce the size and number of macropores in the AASM and increase the porosity, gel pores, and transition pores. However, as the numbers of gel and transition pores increase, the capillary stress generated by the formation of the bending surface is enhanced, resulting in greater autogenous shrinkage of the composite system.

## 3.4 Test optimization and validation

Numerical RSM was used to determine the optimal mix proportion of AASM. $Na_2O$ content, activator modulus, and metakaolin content were selected as independent factors, and compressive strength (28 days) and autogenous shrinkage (14 days) were selected as dependent variables. After ANOVA, set factors, and reaction criteria, see Table 5. According to the predetermined optimization criteria (Table 5), optimization analysis was conducted via RSM, and the optimal combinations of target responses are shown in Table 6. Considering the experimental values of compressive strength and autogenous shrinkage, the optimum mix ratios determined from the 17 groups of experiments designed by RSM is as follows: 6% $Na_2O$ content, 1.5 activator modulus, and 25% metakaolin content.

Five parallel tests were performed under optimal conditions to verify the accuracy of the prediction model, and the findings are shown in Table 7. The relative errors between the experimental and predicted values of compressive strength (at 28 days) and autogenous shrinkage (at 14 days) are 0% and 0.18%, respectively; both errors are less than 5%, indicating that the model has high accuracy. The applicability of the model to the prediction of the compressive strength and autogenous shrinkage of AASM was verified from a mathematical point of view, which offers a certain reference value for the optimization of the ratios of AASM.

# 5 Conclusion

The effects of interactions among $Na_2O$ content, activator modulus, and metakaolin content on the compressive strength

TABLE 5 Criteria for optimization.

| Factor/Response | Lower and upper limits of factors | Criteria for optimization |
|---|---|---|
| $Na_2O$ content (%) | 4–8 | In range |
| Activator modulus | 1.0–2.0 | In range |
| Metakaolin content (%) | 0–50 | In range |
| Compressive strength (MPa) | 3.26–98.5 | Maximize |
| Autogenous shrinkage ($\mu m \cdot m^{-1}$) | 18.17–2316.34 (absolute value) | Minimize |

TABLE 6 Optimal combinations of target responses.

| $Na_2O$ content (%) | Activator modulus | Metakaolin content (%) | Compressive strength (MPa) | Autogenous shrinkage ($\mu m \cdot m^{-1}$) | Desirability |
|---|---|---|---|---|---|
| 6 | 1.5 | 25 | 81.84 | — | 0.953 |
| 4 | 1.5 | 25 | — | −40.794 | 0.998 |

TABLE 7 Verification test results of response surface prediction model.

| Dependent variable | Compressive strength (MPa) | Autogenous shrinkage ($\mu m \cdot m^{-1}$) |
|---|---|---|
| Predicted value | 81.84 | −186.27 |
| Actual value | 82 | −185.5 |
| | 83.4 | −192.5 |
| | 82.4 | −189.5 |
| | 81.4 | −183.5 |
| | 80 | −180.5 |
| Average value | 81.84 | −186.3 |
| Error (%) | 0 | 0.18 |

and autogenous shrinkage of AASM were studied by three-factor, three-level RSM. The phase compositions, microstructures, and pore structures of the cementitious composite materials were analyzed by FTIR, SEM, and MIP. The main conclusions are as follows:

1) Based on the Box–Behnken experimental design, a mathematical model of the effects of the interactions of $Na_2O$ content, activator modulus, and metakaolin content on the compressive strength (at 28 days) and autogenous shrinkage (at 14 days) of AASM was established; the multiple correlation coefficients of the model are 0.9961 and 0.9965, respectively. A comparative analysis of the experimental and predicted values of the AASM shows that the values predicted by the model agree well with the measured values, which proves that the prediction model has high prediction accuracy and good validity.
2) ANOVA and response surface analysis findings reveal that the interactions between Na2O and metakaolin contents and between activator modulus and metakaolin content are the dominant factors affecting the compressive strength and autogenous shrinkage, respectively, of the AASM.
3) Under the interaction of the activator modulus and metakaolin content, the $Ca^{2+}$, $A1^{3+}$, and $Si^{4+}$ ions in the system react with a large number of $[SiO_4]^{4-}$ groups to generate more C-A-S-H and N-A-S-H gels, which fill each other, thereby making the composite structure more compact. Under the interaction of $Na_2O$ and metakaolin contents, the $OH^-$ and $Na^+$ in the solution react with $A1^{3+}$ and $Si^{4+}$ to generate more N-A-S-H, which reduces the compressive strength of the composite system but decreases autogenous shrinkage and increases volume stability.
4) With the compressive strength and autogenous shrinkage of AASM as the optimization goals, the optimal ratios of such materials are as follows: $Na_2O$ content of 6%, activator

modulus of 1.5, and metakaolin content of 25%. Under these optimal conditions, the relative errors between the measured compressive strength and autogenous shrinkage and the values predicted by the model are 0% and 0.18%, respectively. Both errors are less than 5%, indicating that the prediction model has high accuracy and reliability. Moreover, the research of this work provides a theoretical basis for the composition design of AASM composite cementitious materials.

## Data availability statement

The original contributions presented in the study are included in the article/supplementary material, further inquiries can be directed to the corresponding author.

## Author contributions

Conceptualization, JZ and BF; methodology, ZC; software, ZC and HuL. (Huang Li); validation, JZ, BF; ZC and HoL; formal analysis, ZC; investigation, HuL; resources, BF; data curation, JZ; writing—original draft preparation, JZ; writing—review and editing, BF; visualization, HoL; supervision, BF; project administration, BF; funding acquisition, BF. All authors have read and agreed to the published version of the manuscript.

## Funding

This work was supported by the National Natural Science Foundation of China (numbers 51668001), Natural Science Foundation of Ningxia (numbers 2021AAC03187), Key research and development program of Ningxia (numbers 2020BDE03009).

## Conflict of Interest

Author HL was employed by China Construction Fifth Engineering Division Corp.,Ltd. Author BF was employed by Ningxia Coal Industry Co. Ltd.

The remaining authors declare that the research was conducted in the absence of any commercial or financial relationships that could be construed as a potential conflict of interest.

## Publisher's note



## References

Abdelaziz, H., Elhem, G., and George, W. (2019). Optimization approach of granulated blast furnace slag and metakaolin based geopolymer mortars. *Constr. Build. Mat.* 198, 10–26. doi:10.1016/j.conbuildmat.2018.11.251

Antonio, A., Melo, N., Maria, A., and Wellington, R. (2008). Drying and autogenous shrinkage of pastes and mortars with activated slag cement. *Cem. Concr. Res.* 38 (4), 565–574. doi:10.1016/j.cemconres.2007.11.002

ASTM C1698-2009 (2009). *Standard test method for autogenous strain of cement paste and mortar*. West Conshohocken, PA, USA: ASTM International.

Auta, M., and Hameed, B. H. (2011). Optimized waste tea activated carbon for adsorption of Methylene Blue and Acid Blue 29 dyes using response surface methodology. *Chem. Eng. J.* 175, 233–243. doi:10.1016/j.cej.2011.09.100

Barbosa, V., MacKenzie, K., and Thaumaturgo, C. (2000). Synthesis and characterisation of materials based on inorganic polymers of alumina and silica: sodium polysialate polymers. *Int. J. Inorg. Mater.* 2 (4), 309–317. doi:10.1016/S1466-6049(00)00041-6

Bernal, S. A., Provis, J. L., Rose, V., and Gutierrez, R. M. D. (2011). Evolution of binder structure in sodium silicate-activated slag-metakaolin blends. *Cem. Concr. Compos.* 33 (1), 46–54. doi:10.1016/j.cemconcomp.2010.09.004

Burciaga-Díaz, O., Magallanes-Rivera, R. X., and Escalante-García, J. I. (2013). Alkali-activated slag-metakaolin pastes: Strength, structural, and microstructural characterization. *J. Sustain. Cement-Based Mater.* 2 (2), 111–127. doi:10.1080/21650373.2013.801799

Chen, K., Wu, D., Xia, L., Cai, Q., and Zhang, Z. (2021). Geopolymer concrete durability subjected to aggressive environments – a review of influence factors and comparison with ordinary Portland cement. *Constr. Build. Mat.* 279, 122496. doi:10.1016/j.conbuildmat.2021.122496

Chen, X. (2018). *Research on the controlling of setting time of slag-metakaolin geopolymer*. Chongqing: Chongqing University. [master's thesis].

Chen, Y., Zhou, C., Song, B., and Qing, H. (2014). Chemical shrinkage and autogenous shrinkage of cement paste with mineral admixtures added. *J. Build. Mater.* 17 (03), 481–486. doi:10.3969/j.issn.1007-9629.2014.03.020

Chi, M., and Huang, R. (2013). Binding mechanism and properties of alkali-activated fly ash/slag mortars. *Constr. Build. Mat.* 40, 291–298. doi:10.1016/j.conbuildmat.2012.11.003

Cui, C., Peng, H., Liu, Y., Zhang, J., Cai, C., and Peng, A. (2017). Influence of GGBFS content and activator modulus on curing of metakaolin based geopolymer at ambient Temperature). *J. Build. Mater.* 20 (04), 535–542. doi:10.3969/j.issn.1007-9629.2017.04.008

Davidovits, J. (1989). Geopolymers and geopolymeric materials. *J. Therm. Analysis* 35 (2), 429–441. doi:10.1007/BF01904446

Duxson, P., Provis, J. L., Lukey, G. C., Mallicoat, S. W., Kriven, W. M., and Deventer, J. S. J. V. (2005). Understanding the relationship between geopolymer composition, microstructure and mechanical properties. *Colloids Surfaces A Physicochem. Eng. Aspects* 269 (1-3), 47–58. doi:10.1016/j.colsurfa.2005.06.060

Frank, W., Andreas, L., Martin, L., Pavel, S., and Markus, N. (2009). Assessment of phase formation in alkali activated low and high calcium fly ashes in building materials. *Constr. Build. Mat.* 24 (6), 1086–1093. doi:10.1016/j.conbuildmat.2009.11.007

Fu, B., Cheng, Z., and Han, J. (2018). Experimental study on permeability of alkali activ-ated fly ash-slag concrete. *Bull. Chin. Ceram. Soc.* 37 (07), 2255–2259. doi:10.16552/j.cnki.issn1001-1625.2018.07.031

Fu, B., Cheng, Z., Han, J., and Li, N. (2021). Understanding the role of metakaolin towards mitigating the shrinkage behavior of alkali-activated slag. *Materials* 14 (22), 6962. doi:10.3390/MA14226962

Fu, Y., Cai, L., Cao, D., and Wu, Y. (2010). Manufacturing process and properties of alkali-slag Mineral polymer concrete. *J. Build. Mater.* 13 (04), 524–528. doi:10.3969/j.issn.1007-9629.2010.04.022

Gao, Y., Xun, J., Zhang, G., and Fan, J. (2016). Response surface on early performance of alkali-activated slag binder. *J. Build. Mater.* 19 (02), 209–213+220. doi:10.3969/j.issn.1007-9629.2016.02.001

GB/T 17671-2021 (2021). *Method of testing cements-Determination of Strength*. Beijing, China: National Standards of the People's Republic of China.

Guo, J. (2004). *The theoretical research of the pore structure and strength of concrete*. Zhejiang: Zhejiang University. [master's thesis].

Hansen, W. (1987). Drying shrinkage mechanisms in portland cement paste. *J. Am. Ceram. Soc.* 70 (5), 323–328. doi:10.1111/j.1151-2916.1987.tb05002.x

Jiang, W. (2016). *Research on composition and performance of geopolymer based on metakaolin and slag*. Shenyang: Shenyang Jianzhu University. [master's thesis].

Khan, M. I., Sutanto, M. H., Napiah, M. B., Khan, K., and Rafiq, W. (2020). Design optimization and statistical modeling of cementitious grout containing irradiated plastic waste and silica fume using response surface methodology. *Constr. Build. Mat.* 271, 121504. doi:10.1016/J.CONBUILDMAT.2020.121504

Lao, D., Ding, S., Ni, W., Xun, C., Li, X., and Ma, N. (2018). Preparation polysilicate aluminum ferric coagulant from solid waste which containing aluminum, iron and silicon: Responsesurface method optimination and microstructure characteriation. *China's Environ. Sci.* 38 (10), 3720–3728. doi:10.19674/j.cnki.issn1000-6923.2018.0403

Li, G., Cao, H., Weng, L., and Yang, H. (2013). Effect of slag characteristics on performance of cementious inorganic polymer. *concrete* 05, 72–75. doi:10.3969/j.issn.1002-3550.2013.05.020

Li, J., Zhang, W., Li, C., and Monteiro, P. (2020). Eco-friendly mortar with high-volume diatomite and fly ash: Performance and life-cycle assessment with regional variability. *J. Clean. Prod.* 261, 121224. doi:10.1016/j.jclepro.2020.121224

Li, N., Farzadnia, N., and Shi, C. (2017a). Microstructural changes in alkali-activated slag mortars induced by accelerated carbonation. *Cem. Concr. Res.* 100, 214–226. doi:10.1016/j.cemconres.2017.07.008

Li, N., Shi, C., Wang, Q., Zhang, Z., and Ou, Z. (2017b). Composition design and performance of alkali-activated cements. *Mat. Struct.* 50 (3), 178. doi:10.1617/s11527-017-1048-0

Li, N., Shi, C., Zhang, Z., Zhu, D., Hwang, H., Zhu, Y., et al. (2018). A mixture proportioning method for the development of performance-based alkali-activated slag-based concrete. *Cem. Concr. Compos.* 93, 163–174. doi:10.1016/j.cemconcomp.2018.07.009

Li, S., Liu, H., Yang, Y., Li, Q., Zhang, Z., and Zhu, X. (2021). Mechanisms of drying shrinkage for alkali-activated slag/metakaolin composite materials. *Mater. Rep.* 35 (04), 4088–4091. doi:10.11896/cldb.19070067

Liao, Y., Cai, W., Zhang, X., and He, J. (2017). Effect of fly ash on electrical resistivity and chemical shrinkage of cement pastes. *Bull. Chin. Ceram. Soc.* 36 (6), 2059–2063. doi:10.16552/j.cnki.issn1001-1625.2017.06.042

Lin, T., Wang, C., Yousfani, S. H., Wang, W., Qian, X., and Xun, Z. (2018). Study on extraction technology of bamboo fiber by response surface. *Acta Mater. Compos. Sin.* 35 (04), 876–884. doi:10.13801/j.cnki.fhclxb.20170628.001

Liu, S., Wang, F., Li, G., Liu, G., Wang, J., and Qi, Z. (2021). Optimization of mixture ratio and microstructure influence mechanism of composite filling slurry based on response surface method). *Acta Mater. Compos. Sin.* 38 (08), 2724–2736. doi:10.13801/j.cnki.fhclxb.20201013.001

Luo, S., Zhao, M., Jiang, Z., Liu, S., Yang, L., Mao, Y., et al. (2022). Microwave preparation and carbonation properties of low-carbon cement. *Constr. Build. Mat.* 320, 126239. doi:10.1016/J.CONBUILDMAT.2021.126239

Luo, X. C. (2016). *Preparation and properties of slag/metakaolin based geopolymer materials*. Jingdezhen: Jingdezhen Ceramic University. [master's thesis].

Ma, G., Wang, D., Zhong, W., and Fan, L. (2019). The effects of GGBS and Modulus of water glass on the hardening behavior of metakaolin based geopolymer under normal temperature curing. *J. Exp. Mech.* 34 (05), 767–774.

Nedeljkovi, M. (2019). Carbonation mechanism of alkali-activated fly ash and slag materials - in view of long-term performance predictions. Available at: https://research.tudelft.nl/en/publications/carbonation-mechanism-of-alkali-activated-fly-ash-and-slag-materi.doi:10.4233/uuid:97b9eabe-159e-43e1-8b35-edc61b1aa682

Palumbo, G., Iadicicco, A., Messina, F., Ferone, C., Campopiano, S., Cioffi, R., et al. (2018). Characterization of early age curing and shrinkage of metakaolin-based inorganic binders with different rheological behavior by fiber Bragg grating sensors. *Materials* 11 (1), 10. doi:10.3390/ma11010010

Parveen, V., Ankur, M., and Saloni, A. (2019). Effect of ultra-fine slag on mechanical and permeability properties of Metakaolin-based sustainable geopolymer concrete. *Adv. Concr. Constr.* 7 (4), 231–239. doi:10.12989/acc.2019.7.4.231

Paulo, H. R., Banthia, N., Himad, A., Wander, L., and Eduardo, H. M. (2016). Performance of blended metakaolin/blastfurnace slag alkali-activated mortars. *Cem. Concr. Compos.* 71, 42–52. doi:10.1016/j.cemconcomp.2016.04.008

Peng, H., Li, Y., Luo, D., Liu, Y., and Cai, C. (2020). Analysis of reaction level and factors of alkali activated metakaolin/GGBFS. *J. Build. Mater.* 23 (06), 1390–1397.

Provis, J. L. (2013). Geopolymers and other alkali activated materials: Why, how, and what? *Mat. Struct.* 47 (1), 11–25. doi:10.1617/s11527-013-0211-5

Pu, X. (2010). *Alkali slag cement and concrete*. Beijing: Science Press.

Puertas, F., Palacios, M., Manzano, H., Dolado, J. S., Rico, A., and Rodríguez, J. (2011). A model for the C-A-S-H gel formed in alkali-activated slag cements. *J. Eur. Ceram. Soc.* 31 (12), 2043–2056. doi:10.1016/j.jeurceramsoc.2011.04.036

Ren, J., Zhang, L., and San Nicolas, R. (2020). Degradation process of alkali-activated slag/fly ash and Portland cement-based pastes exposed to phosphoric acid. *Constr. Build. Mat.* 232, 117209. doi:10.1016/j.conbuildmat.2019.117209

Ren, J., Zhang, L., Walkley, B., Black, J. R., and San Nicolas, R. (2022a). Degradation resistance of different cementitious materials to phosphoric acid attack at early stage. *Cem. Concr. Res.* 151, 106606. doi:10.1016/J.CEMCONRES.2021.106606

Ren, J., Zhang, L., Zhu, Y., Li, Z., and San Nicolas, R. (2022b). A comparative study on the degradation of alkali-activated slag/fly ash and cement-based mortars in phosphoric acid. *Front. Mat.* 9. doi:10.3389/FMATS.2022.845349

Rynel, I. (2015). *Patent issued for materials comprising water-soluble polymer particles and methods of making and using them*. Boston: Biotech Week.

Shengtu, Q., Qian, X., and Qian, K. (2019). Research on compressive strength and microstructure of bottom ash based geopolymer. *New Build. Mater.* 46 (05), 67–70+75.

Shervin, A., and Soheil, K. (2018). Multi-objective optimization of influential factors on production process of foamed concrete using Box-Behnken approach. *Constr. Build. Mat.* 170, 101–110. doi:10.1016/j.conbuildmat.2018.02.189

Sui, J., and Liu, X. (2013). Preparation and characterization of a dual-layer carbon film on 6H-SiC wafer using carbide-derived carbon process with subsequent chemical vapor deposition. *Surf. Coat. Technol.* 235, 469–474. doi:10.1016/j.surfcoat.2013.08.005

Susan, B., Ruby, D. G., Silvio, D., and Erich, R. (2007). Performance of an alkali-activated slag concrete reinforced with steel fibers. *Constr. Build. Mat.* 24 (2), 208–214. doi:10.1016/j.conbuildmat.2007.10.027

Wan, Q., Rao, F., Song, S., Ramiro, E., Ricardo, G., Patino, C. L., et al. (2017). Geopolymerization reaction, microstructure and simulation of metakaolin-based geopolymers at extended Si/Al ratios. *Cem. Concr. Compos.* 79, 45–52. doi:10.1016/j.cemconcomp.2017.01.014

Wang, A., Sun, D., Hu, P., and Reng, X. (2008). Experimental research on preparing geopolymeric cement with metakaolin activated by alkali activators. *J. Hefei Univ. Technol.* 2008 (04), 617–621. doi:10.3969/j.issn.1003-5060.2008.04.031

Wang, D. (2018). *Research on shrinkage characteristics of alkali slag/fly ash composite cementitious materials*. Anhui: Anhui University of Science and Technology. [master's thesis].

Yang, T., Yao, X., Gu, G., and Zhu, H. (2015). Effects of slag on reaction and composition of alkali-activated fly ash-slag blends. *J. Nanjing Univ. Technol. Sci. Ed.* 37 (05), 19–26. doi:10.3969/j.issn.1671-7627.2015.05.004

Yang, T., Zhu, H., and Zhang, Z. (2017). Influence of fly ash on the pore structure and shrinkage characteristics of metakaolin-based geopolymer pastes and mortars. *Constr. Build. Mat.* 153 (30), 284–293. doi:10.1016/j.conbuildmat.2017.05.067

Yang, X. (2020). *Study on the mechanism of alkali activated fly ash/slag autogenous shrinkage*. Guangzhou: Guangzhou University. [master's thesis].

Yang, X., Yang, Z., Gao, Q., and Chen, D. (2016). Cemented filling strength test and optimal proportion decision of mixed filling aggregate. *Rock Soil Mech.* 37 (S2), 635–641. doi:10.16285/j.rsm.2016.S2.080

Yip, C. K., Lukey, G. C., and Deventer, J. S. J. (2004). The coexistence of geopolymeric gel and calcium silicate hydrate at the early stage of alkaline activation. *Cem. Concr. Res.* 35 (9), 1688–1697. doi:10.1016/j.cemconres.2004.10.042

Zarina, Y., Al Bakri Abdullah, M. M., Kamarudin, H., Khairul, N. I., and Abd, R. R. (2012). Reviews on the geopolymer materials for coating application. *Adv. Mat. Res.* 626, 958–962. doi:10.4028/www.scientific.net/amr.626.958

Zhan, J., Li, H., Pan, Q., Cheng, Z., Li, H., and Fu, B. (2022). Effect of slag on the strength and shrinkage properties of metakaolin-Based geopolymers. *Materials* 15 (8), 2944. doi:10.3390/MA15082944

Zhang, H., Huang, X., Zong, Z., and Tang, G. (2017). Optimization of preparation program for hexadecanol-palmitic acid-lauric acid/$SiO_2$ composite materials by response surface methodology based on heat and moisture comprehensive property. *Acta Mater. Compos. Sin.* 34 (01), 203–209. doi:10.13801/j.cnki.fhclxb.20160322.003

Zhang, Q., Li, X., and Yang, W. (2013). Optimization of filling slurry ratio in a mine based on back-propagation neural network. *J. Central South Univ. Technol.* 44 (07), 2867–2874.

Zhang, Z., Li, L., Ma, X., and Wang, H. (2016). Compositional, microstructural and mechanical properties of ambient condition cured alkali-activated cement. *Constr. Build. Mat.* 113 (15), 237–245. doi:10.1016/j.conbuildmat.2016.03.043

Zhao, X. (2013). *Test design method*. Beijing: Science Press, 204–209.

Zheng, W., and Zhu, J. (2015). *Structure engineering application foundation of alkali slag cementitious material*. Harbin: Harbin Institute of Technology Press, 1–53.

Zhong, Q., Su, M., and Peng, H. (2021). Experiment and Lasso regression model of the macroscopic performance of metakaolin-slaggeopolymer paste. *Acta Mater. Compos. Sin.* 2021, 1–13. doi:10.13801/j.cnki.fhclxb.20200000.000000

Zhou, Y., Xie, L., Kong, D., Peng, D., and Zheng, T. (2022). Research on optimizing performance of desulfurization-gypsum-based composite cementitious materials based on response surface method. *Constr. Build. Mat.* 341, 127874. doi:10.1016/J.CONBUILDMAT.2022.127874

Zhu, X., Kang, X., Deng, J., Yang, K., Jiang, S., and Yang, C. (2021). Chemical and physical effects of high-volume limestone powder on sodium silicate-activated slag cement (AASC). *Constr. Build. Mat.* 292, 123257. doi:10.1016/J.CONBUILDMAT.2021.123257

Zhu, X., Tang, D., Yang, K., Zhang, Z., Li, Q., Pan, Q., et al. (2018). Effect of $Ca(OH)_2$ on shrinkage characteristics and microstructures of alkali-activated slag concrete. *Constr. Build. Mat.* 175, 467–482. doi:10.1016/j.conbuildmat.2018.04.180